Nonthermal Ablation by Using Intravascular Oxygen Radical Generation with WST11: Dynamic Tissue Effects and Implications for Focal Therapy[1]

Simon Y. Kimm, MD
Tatum V. Tarin, MD
Sébastien Monette, DMV
Govindarajan Srimathveeravalli, PhD
Daniel Gerber, BS
Jeremy C. Durack, MD
Stephen B. Solomon, MD
Peter T. Scardino, MD
Avigdor Scherz, PhD
Jonathan Coleman, MD

Purpose: To examine the hypothesis that vascular-targeted photodynamic therapy (VTP) with WST11 and clinically relevant parameters can be used to ablate target tissues in a non–tumor-bearing large-animal model while selectively sparing blood vessels and collagen.

Materials and Methods: By using an institutional animal care and use committee–approved protocol, 68 ablations were performed in the kidneys (cortex and medulla) and livers of 27 adult pigs. Posttreatment evaluation was conducted with contrast material–enhanced computed tomography in the live animals at 24 hours. Immunohistochemistry was evaluated and histologic examination with hematoxylin-eosin staining was performed at 4 hours, 24 hours, and 7 days. Intravenous infusion of WST11 (4 mg per kilogram of body weight) was followed by using near-infrared illumination (753 nm for 20 minutes) through optical fibers prepositioned in target tissues by using a fixed template. Treated areas were scanned, measured, and statistically analyzed by using the Student *t* test and two-way analysis of variance.

Results: Focal WST11 VTP treatment in the liver and kidney by using a single optical fiber resulted in well-demarcated cylindrical zones of nonthermal necrosis concentrically oriented around the light-emitting diffuser, with no intervening viable parenchymal cells. The radius of ablated tissue increased from approximately 5 mm at 150 mW to approximately 7 mm at 415 mW ($P < .01$). Illumination through fiber triads at 1-cm separation resulted in confluent homogeneous necrosis. Patterns of acute injury within 24 hours were consistent with microcirculatory flow arrest and collagen preservation (demonstrated with trichrome staining). In the peripheral ablation zone, blood vessels at least 40 μm in diameter were selectively preserved and remained functional at 7 days. Ablated tissues exhibited progressive fibrosis and chronic inflammatory cell infiltrates. No histologic changes consistent with thermal injury were observed in blood vessels or collagen. The renal hilum and collecting system did not show treatment effect, despite treatment proximity.

Conclusion: WST11 VTP induces nonthermal tissue ablation in target tissue while preserving critical organ structures and bystander blood vessels within solid organs.

Online supplemental material is available for this article.

[1] From the Urology Service, Department of Surgery (S.Y.K., D.G., P.T.S., J.C.), Tri-Institutional Laboratory of Comparative Pathology, Rockefeller University, Weill Cornell Medical College (S.M.), Radiochemistry and Imaging Sciences Service (G.S.), and Interventional Radiology Service (J.C.D., S.B.S.), Department of Radiology, Memorial Sloan Kettering Cancer Center, 1275 York Ave, New York, NY 10065; Department of Urology, University of Pittsburgh Medical Center, Pittsburgh, Pa (T.V.T.); and Department of Plant Sciences, Weizmann Institute of Science, Rehovot, Israel (A.S.). Received July 16, 2014; revision requested September 15; revision received June 15, 2015; accepted July 7; final version accepted January 12, 2016. **Address correspondence to** J.C. (e-mail: *colemanj@mskcc.org*).

Supported by the Sidney Kimmel Center for Prostate and Urologic Cancers, a National Institutes of Health Core Grant (no. P30 CA008748), and the Wade Thompson Foundation.

Tumor ablation therapies have been used to treat localized cancers with negligible treatment-related morbidity, yet these therapies have major limitations that can impair treatment effectiveness or risk collateral tissue damage (1,2). This is particularly true of thermal tissue ablation technologies, such as radiofrequency ablation, high-intensity focused ultrasound, microwave ablation, and cryotherapy (3–9), in which the heat-sink effect from tissue vascularity (3,10,11) and/or indiscriminant damage to surrounding normal tissues is problematic. Moreover, the nonselectivity of tissue destruction at therapeutic energies, in particular the impairment of collagen scaffold and nontumor blood vessels, is detrimental to the recovery of normal tissue function in or near the target thermal ablation zone (3,12–15). Alternative nonthermal technologies for in situ tissue treatment have been sought to overcome these serious limitations.

To address this need for advancement, we examined the use of a nonthermal form of tissue ablation with vascular-targeted photodynamic therapy (VTP) by using WST11 (Tookad Soluble; Steba Biotech, France) a water-soluble near-infrared–activated compound (16–18) that noncovalently binds to serum albumin and stays sequestered within the circulation until clearance with an elimination half-life of less than 60 minutes in humans (16). As observed in trials with small animals (19), when WST11 is activated by light, super oxide and hydroxyl radicals produced in the blood mediate a cascade of events that resemble profound, transient, and localized ischemia-reperfusion injury that results in a complete tumor vascular arrest, including feeding arteries and draining veins, followed by localized necrosis (19,20). WST11 VTP profoundly differs from classic photodynamic therapy (21–27) and offers major advantages, including absence of prolonged toxicity, a major drawback of classic photodynamic therapy (4,28–30). WST11 VTP was applied successfully and safely in phase II clinical trials in patients with early-stage prostate cancer (31). Evidence of both successful ablation and preserved quality of life suggest that WST11 VTP has the potential to overcome drawbacks of current ablation approaches and effectively treat cancers localized in other organs, such as those near important blood vessels, with minimal damage to surrounding tissues. In our study, we aimed to examine the hypothesis that WST11 VTP with clinically relevant parameters can be used to ablate target tissues in the kidney and liver of a non–tumor-bearing large-animal survival model while selectively sparing noncapillary blood vessels and collagen.

Advances in Knowledge

- Treatment with WST11 vascular-targeted photodynamic therapy (VTP) demonstrates uniform, concentric necrosis consistent with its intravascular, nonthermal mechanism of action.
- The photochemical effect of WST11 VTP in healthy tissues selectively spares normal blood vessels larger than 40 μm in diameter in the periphery of the treatment zone but with complete necrosis of the surrounding parenchymal tissues and without evidence of perivascular tissue sparing.
- Tissue ablation with WST11 VTP spares normal tissue collagen within the ablation zone, suggesting that normal tissue proteins can be preserved.

Implications for Patient Care

- Tissue ablation with WST11 VTP may be useful for treating tumors close to blood vessels, where other forms of thermal ablation are less effective.
- Sparing of normal vessels and tissue collagen with WST11 VTP may provide an opportunity for normal tissue remodeling after treatment, thus minimizing adverse functional effects.

Materials and Methods

Study Design

Our institutional animal care and use committee approved the animal use protocol for this study. All procedures were conducted in accordance with the Guide for the Care and Use of Laboratory Animals. Tissue effects of WST11 VTP ablation at 4 hours, 24 hours, and 7 days after treatment were evaluated in a healthy porcine model. Two solid organs, the kidney and liver, were chosen for their clinical relevance as common sites for ablative therapies. We examined the effects on normal tissue over a range of treatment parameters used in preclinical models and clinical studies of cancer ablation (31,32).

Animal Model

Twenty-seven female Yorkshire pigs that weighed 30–35 kg received food and water ad libitum and were housed for a minimum of 7 days for quarantine, acclimation, and observation prior

Published online before print
10.1148/radiol.2016141571 **Content code:** IR

Radiology 2016; 281:109–118

Abbreviations:
ATN = acute tubular necrosis
CN = coagulative necrosis
H-E = hematoxylin-eosin
HZ = hemorrhage zone
IQR = interquartile range
TUNEL = terminal deoxynucleotidyl transferase dUTP nick end labeling
VTP = vascular-targeted photodynamic therapy

Author contributions:
Guarantors of integrity of entire study, S.Y.K., A.S., J.C.; study concepts/study design or data acquisition or data analysis/interpretation, all authors; manuscript drafting or manuscript revision for important intellectual content, all authors; approval of final version of submitted manuscript, all authors; agrees to ensure any questions related to the work are appropriately resolved, all authors; literature research, S.Y.K., T.V.T., G.S., A.S.; clinical studies, S.Y.K.; experimental studies, S.Y.K., T.V.T., S.M., G.S., D.G., J.C.D., S.B.S., A.S., J.C.; statistical analysis, S.Y.K.; and manuscript editing, S.Y.K., T.V.T., S.M., G.S., J.C.D., S.B.S., P.T.S., A.S., J.C.

Conflicts of interest are listed at the end of this article.

to the procedure. A fentanyl patch (25 mg/hour) was placed 12–14 hours prior to surgery. The night before surgery, the pigs fasted for 12 hours but were allowed water. All pigs were sedated with tiletamine and zolazepam (4.4 mg per kilogram of body weight) and were given glycopyrrolate (0.007 mg per kilogram of body weight). A local infiltrate of bupivacaine (0.25%) was delivered subcutaneously along the midline prior to laparotomy. Each pig was intubated and maintained on isoflurane (1.5%–2.5%) during surgery. A 16-gauge angiocatheter was placed in an ear vein for blood collection and drug administration. Isotonic saline was infused intravenously at a rate of 10–15 mL per kilogram of body weight per hour during the procedure.

Surgical Procedures and WST11 VTP

All procedures, including surgical interventions, fiber placements, and illuminations, were performed by one investigator (S.Y.K.) who had more than 5 years of related surgical experience before conducting these studies. After induction of anesthesia by a trained veterinarian and prior to administration of WST11, a midline laparotomy was performed on each pig, and both kidneys and the liver were exposed (S.Y.K.). The 600-μm illuminating fibers were inserted in atraumatic fashion with a blunt-tip cannula into the kidneys and liver (S.Y.K.) by using templates with multiple fiber configurations (Fig E1 [online]). Within each triangular template, four thermocouples were placed to measure tissue temperature at the center and 3 mm, 5 mm, and 7 mm from the center of each array of fibers to minimize any potential light-shadowing effect. All WST11 delivery devices and intravenous tubing were protected from ambient light.

Photosensitizer and Illumination Source

WST11 was used as described previously (31). Briefly, WST11 was prepared and reconstituted in saline under sterile, light-protected conditions and administered intravenously at a standard dose of 4 mg per kilogram of body weight. Illumination was then provided by a 753-nm medical diode laser (V-Gen, Tel Aviv, Israel) connected to plastic fiber optics (Medlight SA, Écublens, Switzerland), as described previously. The diffuser tip of the optical fiber was inserted into the organ of interest to a minimum depth of 1 cm (S.Y.K.). The upper, middle, and lower pole regions of the kidney were treated with fibers inserted along the lateral aspect of the kidney, directed radially toward the hilum and providing treatment to the cortex and medulla. Fibers inserted into the liver to a minimum depth of 1 cm were arranged in the right lobe at least 5 cm away from the porta hepatis. After secure fiber insertion and intravenous administration of WST11, light was delivered through the fibers for 20 minutes at fluence rates of 75 mW/cm, 100 mW/cm, 150 mW/cm, 208 mW/cm, and 415 mW/cm. In all, 68 ablations performed in 27 animals were included in our study.

Ten animals received liver treatment only, and 17 animals received both kidney and liver treatment (acute model only). Each hepatic and renal ablation zone in all 27 animals was analyzed. In addition, sham treatments (light fiber and illumination only, without WST11) were performed in 10 treatments (10 kidney and 10 liver treatments) and analyzed for each treatment. Computed tomographic (CT) images were obtained by using a multi–detector row CT scanner (LightSpeed 16; GE Healthcare, Milwaukee, Wis).

Laboratory Studies

Laboratory studies included a complete blood count, comprehensive metabolic panel, fibrin, fibrinogen, and coagulation profile and were performed prior to infusion and treatment, then prior to euthanasia. Animals were euthanized with injection of a commercial euthanasia solution that contained sodium pentobarbital and sodium phenytoin (1 mL per 4.5 kg of body weight) while under deep anesthesia 4 hours (n = 6), 24 hours (n = 15), or 7 days (n = 6) after completion of VTP treatment. During necropsy, treatment sites were completely resected, photographed, and measured after sequential immersion in 1, 2, 3, 5-triphenyltetrazolium chloride in phosphate-buffered saline with a pH level of 8.5 (Sigma-Aldrich, St Louis, Mo). Tissues were fixed in 10% neutral-buffered formalin for 72 hours, paraffin embedded, and sectioned to 4-μm thickness and affixed to slides stained with hematoxylin-eosin (H-E) stain. Ablation zones were step-sectioned perpendicular to the long axis at 2-mm intervals for volumetric analysis. Additional sections were obtained from selected specimens for histochemical staining with the Masson trichrome technique for collagen and with the terminal deoxynucleotidyl transferase dUTP nick end labeling (TUNEL) technique, as described previously (33). Selected sections were also stained with immunohistochemistry for cleaved caspase-3 on a Leica Bond RX automated staining platform (Leica Biosystems, Buffalo Grove, Ill). After heat-induced epitope retrieval at a pH level of 6.0, the primary antibody (polyclonal rabbit, catalog no. 9661; Cell Signaling Technology, Beverly, Mass) was applied at a concentration of 1:250 and was followed by application of a polymer detection system (Novocastra Bond Polymer Refine Detection; Leica Biosystems).

A board-certified veterinary pathologist with 13 years of experience (S.M.) performed histologic assessments. Volumetric analysis was performed by using a digitized slide scanner, and measurements were obtained with both digital and optical slide imaging. Aperio ImageScope digital slide imaging software (Aperio, Vista, Calif) was used for volumetric analysis by outlining ablated regions, and three-dimensional reconstructions were then created from digitized step-sections by using three-dimensional Slicer software *(http://www.slicer.org)*.

Statistical Analysis

Sixty-eight ablations were performed, allowing for more than three ablations for each laser fluence and time combination. Ablation volumes were

analyzed as medians with interquartile ranges (IQRs). The short-axis distance (in millimeters) from the illuminating laser fiber and the first viable portal tract was used as a measure of the size of the coagulative necrosis (CN) zone, and medians and IQRs were calculated for each. The Mann-Whitney rank sum test was used to identify significant differences in the groups. Two-sample *t* tests were used to perform pairwise comparisons of each measurement between the ablation groups and to check for differences between the laser fluence groups. Analysis of variance was used to identify significant differences for comparisons of three or more groups. To illustrate the relationship between blood vessel size and blood vessel ablation, 10 liver and 10 kidney ablations were included in the analysis, with 40–50 blood vessels counted on each slide with three to five slides per ablation. All statistical analyses, including the Student *t* test, two-way analysis of variance, and nonparametric tests that included the Wilcoxon and Mann-Whitney rank sum tests, were performed by using Stata Statistical Software version 12.0 (StataCorp, College Station, Tex). All *P* values resulted from the use of two-sided statistical tests, and a *P* value of .05 was considered the threshold to indicate a significant difference.

Results

Macroscopic Observations

Four hours after WST11 VTP ablation, treated regions within the liver and kidney were grossly evident as homogeneous zones of red discoloration (Fig E2 [online]). Nonviability of tissues within ablation zones was confirmed by lack of 1, 2, 3, 5-triphenyltetrazolium chloride staining. This corresponded with areas of necrosis on H-E–stained slides and was confirmed with TUNEL staining. Twenty-four hours after ablation, darker discoloration at the center of each lesion was visible at gross examination and corresponded to regions of CN on H-E–stained slides. Seven days after application of WST11 VTP, the treated zones within both liver and kidney showed regions of central pallor with peripheral red discoloration, which corresponded to regions of fibrosis that were visible on H-E–stained sections. The volume of the ablated domains increased with light fluence and possessed sharp borders. Tissues outside the ablated domains appeared normal at gross inspection and at histologic examination.

Sham treatments (light illumination, no infusion of WST11) performed in 10 animals that received 10 liver and 10 kidney treatments resulted in minimal temperature increases of 1°C –2°C for all light settings (Fig E3 [online]). There was no histologic evidence of tissue effects for sham procedures other than local trauma caused by passage of the fiber cannula. Tissue temperature changes were also negligible with active WST11 VTP conditions at laser energies of 75 and 150 mW/cm. Increase in tissue temperature was seen at light fluences of 208 and 415 mW/cm within the treatment zone. The mean sustained temperature increase during treatment (ΔT[°C]) was +16°C and +11°C at 415 mW/cm and +8°C and +3°C at 208 mW/cm in the liver and kidney, respectively. No temperature change was observed 7 mm away from the array center at all tested fluence rates (Fig E4 [online]).

Histologic Examination of Liver and Kidney Tissues Treated with WST11 VTP

Four hours after ablation.—On H-E–stained slides of liver and kidney tissues, ablation zones were visible concentrically around each laser fiber. Triangular or rectangular fiber arrays produced a coalescent ablation zone between the laser fibers (Fig E2 [online]). In the liver, treated areas demonstrated hyperemia and hemorrhage of hepatic sinusoids and separation of hepatocytes (Fig E5 [online]). Early events of cell death were observed, including condensation of chromatin, and this was supported by positive TUNEL staining.

Similar evidence of early necrotic events was seen in kidney tissues (Fig E6 [online]). Areas of tubular dilation and hyaline casts surrounded ablated regions that showed tissue hyperemia with congestion of renal capillaries. Tubular cells showed early degenerative separation from their basement membranes, and TUNEL-positive staining in the ablation zone was observed. Histologically, tissue at each zone of treatment appeared similar when comparing high (415-mW/cm) and low (150-mW/cm) laser fluences in both liver and kidney without evidence of tissue thermal effects.

Twenty-four hours after ablation.—All treated liver tissues demonstrated well-defined areas of complete CN of all structures, which correlated with fiber placement (Fig 1). Beyond this zone, there was a region of parenchymal necrosis with hemorrhage zone (HZ) and hyperemia. A sharply demarcated border was visible between this zone and normal liver tissue. Bile ducts and hepatocytes in the HZ stained clearly for DNA fragmentation (with TUNEL) and cleaved caspase-3 (Fig 1). No TUNEL or cleaved caspase-3 staining of blood vessel endothelium was observed in the HZ, and the vessels appeared to be preserved despite being completely surrounded by necrotic hepatocytes. Some sporadic, small foci of cleaved caspase-3–stained hepatocytes were observed 1.0–4.6 mm outside the HZ boundary.

Treated kidney tissues showed a similar region of complete CN of all structures concentrically around the laser fiber (Fig E7 [online]), with renal tubules stained by TUNEL for DNA fragmentation and cleaved caspase-3. Beyond this zone, a surrounding peripheral zone of acute tubular necrosis (ATN) with superimposed vascular hyperemia and hemorrhage was observed. Vascular sparing despite complete necrosis of the surrounding parenchymal cells was evident in vessels at least 40 μm in diameter within the ATN zone (Fig E8 [online]). While necrosis of tubules was global and homogenous in the CN zone, the periphery of the ATN regions showed populations of tubules that appeared to be resistant to treatment effects. Proximal tubules of the kidneys appeared more susceptible to

Figure 1

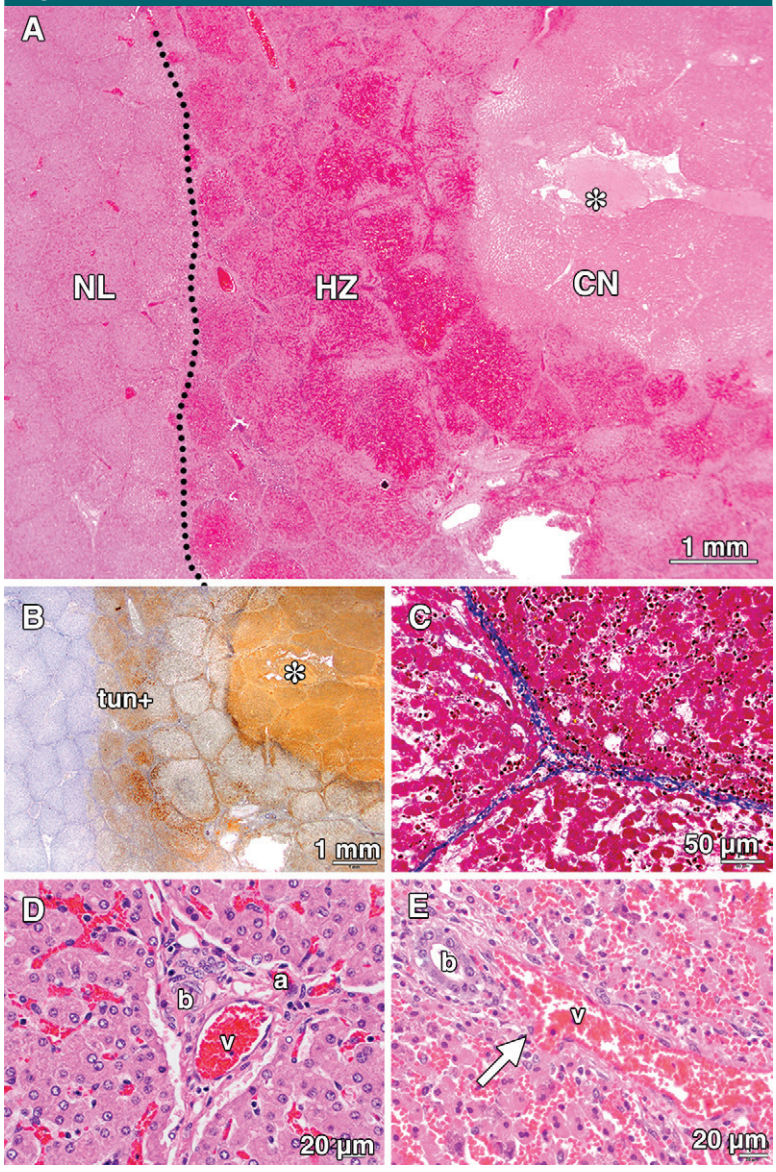

Figure 1: Photomicrographs of porcine liver tissue 24 hours after treatment (with 415 mW). ∗ = position of the laser fiber on each image. *A,* On the H-E–stained section (original magnification, ×10), the treated region is clearly visible as a zone of CN *(CN)* surrounding the laser fiber. This is surrounded by a more peripheral concentric zone defined by parenchymal necrosis and hemorrhage *(HZ).* Within this zone, structures such as arteries, veins, and bile ducts are variably affected. A normal-appearing region *(NL)* is sharply delineated outside the treatment area (indicated by the dotted line). *B,* TUNEL-stained section (original magnification, ×10) shows a dense, well-circumscribed region of necrotic cells with fragmented DNA *(tun+)* homogeneously surrounding the laser fiber. *C,* Photomicrograph obtained after treatment (original magnification, ×40) shows that no changes in the structure of collagen were visible at light microscopy, despite complete ablation and necrosis of surrounding hepatocytes in the CN zone. *D,* High-power view of an H-E–stained section (original magnification, ×400) from the normal-appearing area shows the normal cellular and architectural appearance of a porcine portal triad, consisting of a bile duct *(b),* artery *(a),* and vein *(v). E,* High-power view of an H-E–stained section (original magnification, ×400) from the CN zone shows complete parenchymal necrosis and necrosis of a small 40-μm vein (*v,* arrow) and bile duct *(b).*

necrosis than distal or collecting system tubules. Similar to the HZ region in the liver, vessel preservation in the ATN zone was supported by absent vascular endothelial TUNEL staining. Regions of sublethal tissue injury marked by tubular hyaline casts were also observed. Tissue beyond the sharply demarcated zone of ablation appeared normal and viable. No evidence of injury to the renal hilar vessels was observed (Fig E9 [online]), despite the close proximity to treated regions.

With increasing laser energy, there was an increase in the size of the ablated region. Volumetric analysis of liver step-sections demonstrated significant differences ($P < .01$) in lesion volume between low (100-mW/cm) and high (415-mW/cm) energy fluences (Fig 2). The overall volume of the ablated tissue (V_a in the following equation) increased at approximately the square root of the light fluence *(f),* such that $V_{a2} \sim V_{a1} \cdot \sqrt{(f_2/f_1)}$, where f_2 and f_1 are the light fluencies (in milliwatts per centimeter) resulting in ablated volumes V_{a2} and V_{a1}, respectively. Although ablation volumes differed, the histologic characteristics of lesions created at different light fluences remained similar. This statement is based on a careful comparison of the histologic changes for each ablated zone observed after WST11 VTP treatment with high and low laser fluence. In particular, the percentage of ablation that consisted of CN seen within the ablated zone after at least 24 hours remained constant (Fig E10 [online]). Tissues that underwent sham treatment did not show any histologic evidence of ablation injury.

In sharp contrast to the tissues that underwent thermal ablation, trichrome staining of the treated tissues at 24 hours showed no indication of collagen scaffold impairment (Fig E11 [online]).

Seven days after ablation.—Seven days after WST11 VTP ablation, H-E–stained slides of liver and kidney tissues exhibited progressive fibrosis and evidence of tissue remodeling, accompanied by infiltration of chronic inflammatory cells, such as macrophages and monocytes. The encroachment of fibrosis appeared directional,

Figure 2

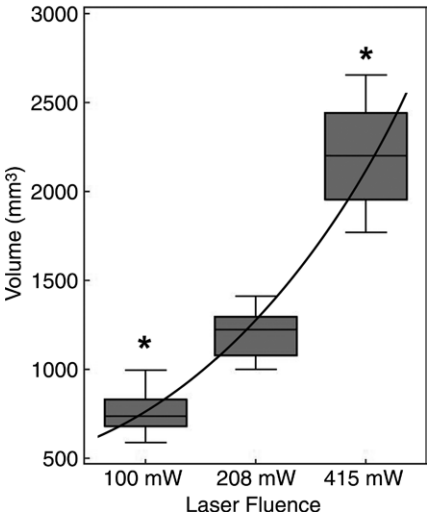

Figure 2: Plot of liver lesion volume (in cubic millimeters) as a function of laser fluence 24 hours after WST11 VTP. At 100 mW ($n = 15$; mean, 767.5 mm^3; median, 738.85 mm^3; IQR, 681.45–834.03 mm^3), 200 mW ($n = 12$; mean, 1204.03 mm^3; median, 1227.62 mm^3; IQR, 1081.65–1294.91 mm^3), and 415 mW ($n = 18$; mean, 2209.84 mm^3; median, 2204.01 mm^3; IQR, 1957.35–2443.12 mm^3), higher fluences resulted in larger lesion volumes. * = statistical significance ($P < .0001$ with the Mann-Whitney rank sum test).

Figure 3

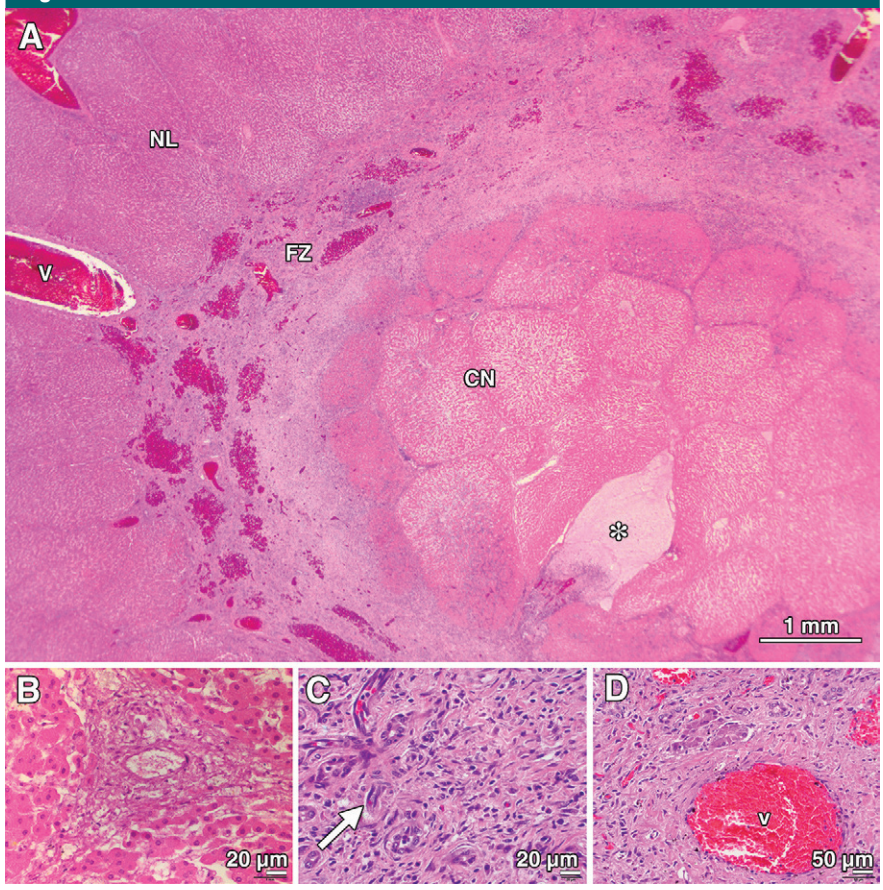

Figure 3: Photomicrographs (H-E stain) of porcine liver tissue 7 days after treatment (with 415 mW). * = position of the laser fiber on each image. *A,* Photomicrograph (original magnification, ×10) shows that the treated area consisted of an area of CN surrounding the path of the laser fiber, surrounded by a region of fibrotic tissue *(FZ)* contraction. Residual areas of hemorrhage persisted in this concentric ring of fibrosis that appeared to encroach on the lesion from the periphery. A normal-appearing region *(NL)* was sharply delineated outside the treatment area, with an intact vein *(v)* in the field. *B,* High-power view (original magnification, ×400) from the CN region of the treated area shows ablation of hepatocytes and necrosis of the bile ducts and vessels within the portal triad. *C,* High-power view (original magnification, ×400) from the zone of fibrosis shows increased density of preexisting blood vessels that were viable after treatment, along with immature blood vessels (arrow) that are suggestive of neovascularization. The region is infiltrated with chronic inflammatory cells. *D,* Photomicrograph (original magnification, ×200) shows a portal triad that contains an intact blood vessel *(v)* in the periphery of the fibrotic zone is pictured, indicating sparing of the structure after treatment.

progressing from the periphery toward the center of each ablated area, with residual central areas of CN (Fig 3). Viable blood vessels within the HZ, as described earlier, persisted. Areas of increased blood vessel and bile duct density were visible, along with evidence of angiogenesis. Findings were consistent with hepatocyte destruction and resorption, with persistence of preserved blood vessels. Where triads of laser fibers were deployed, a triangular region of necrosis was created with fibrotic encroachment that developed from the periphery into the coalescent CN zone of each lesion (Fig E12 [online]). In the kidney, a similar pattern of chronic inflammation and fibrosis was seen, including areas of increased blood vessel density (Fig 4, Fig E13 [online]).

Laboratory testing for alterations in complete blood count, serum chemistry levels (sodium, potassium, CO_2, chlorine, blood urea nitrogen, creatinine, and glucose levels), and coagulation pathway indicators (prothrombin time, partial thromboplastin time, and fibrinogen) were measured, and no significant alterations were seen at each time point between sham animals and treated animals. This corroborates findings from other preclinical studies of WST11 VTP (34).

Effect of WST11 VTP on Blood Vessels in Normal Tissues

Vessels of the microcirculation, such as the blood vessels of the liver portal tracts and sinusoids, appeared ablated within the CN region and were spared farther away from the source of illumination (Fig E14 [online]). In the HZ region of the liver and the ATN region of the kidney, blood vessels at least 40 μm

Figure 4

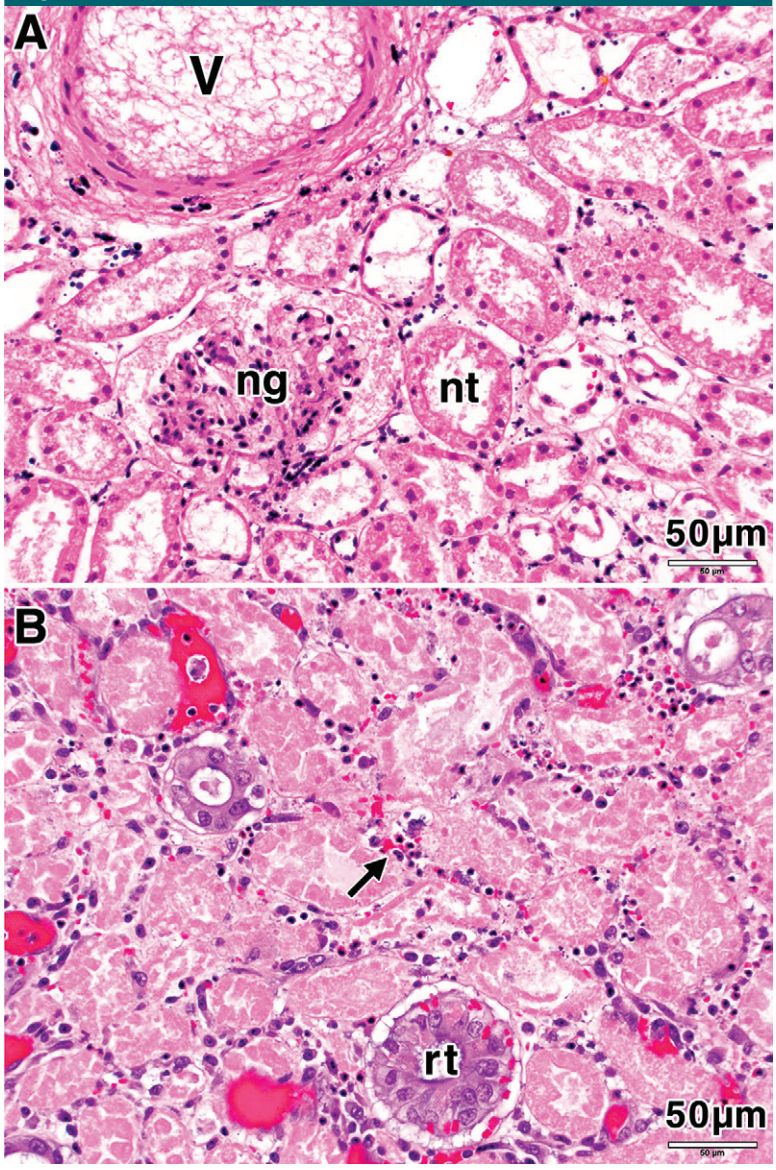

Figure 4: Photomicrographs (H-E stain; original magnification, ×100) of porcine kidney tissue 7 days after treatment (with 415 mW). *A,* High-power view of the treatment zone shows necrosis of kidney tubules *(nt),* a necrotic glomerulus *(ng),* and a necrotic blood vessel *(v). B,* High-power view in the zone of fibrotic change shows regenerating tubules *(rt)* and inflammatory infiltrate (arrow).

in diameter were spared, although the parenchymal cells that surrounded them were fully necrotic. The distance between the laser fiber and the first spared vessels smaller than 40 μm in diameter appeared to increase linearly with increasing light fluence (*f* in the following equation), such that $r_{s2} = f_2/f_1 r_{s1}$, where r_{s1} and r_{s2} are the radii of the ablated zones due to illumination with f_1 and f_2 light fluencies, respectively (Fig 5). No vascular thrombosis was visible in the treated regions, according to the H-E–stained slides.

In the kidney, WST11 VTP ablations of medullary regions that extended into the highly vascular renal hilum showed no effect on the primary and segmental arteries and veins that enter the kidney (Fig E9 [online]). Contrast-enhanced imaging showed no devascularized areas outside of the ablation zone (Fig E9 [online]). Laboratory analysis demonstrated no significant alterations to global renal function, and no perforation of the collecting system or vessels was observed.

Discussion

The shortcomings of thermal ablation have encouraged the search for nonthermal approaches that prevent the heat-sink effect and/or enhance treatment effectiveness with less morbidity to nearby normal tissues and organs. Application of WST11 VTP to animal and human cancers in preclinical and clinical trials, respectively, has shown tumor vascular collapse, including feeding arteries and draining veins (35,36), accompanied by necrotic cell death and subsequent tumor eradication (29,36). Examination of the surrounding noncancerous tissue in small-animal models suggested sparing of the normal blood vessels (32,36). Likewise, examination of prostate biopsy specimens obtained 6 months after hemiablation with WST11 VTP for treatment of early-stage cancers showed sparing of large normal vessels in the treatment zone (29,31). Preservation of collagenous structures, such as the capsule and the urethra, was demonstrated with both magnetic resonance imaging and patient physiological status reported 1 and 6 months after treatment (28). Moreover, the absence of incontinence after treatment was indicative of muscle intactness under the treatment conditions. Additional preclinical studies with WST11 VTP were performed in the prostates of non–tumor-bearing dogs, and prostate histologic examination was performed 1 week after treatment. However, fibrosis in the HZ had already occurred, leaving only the central CN for inspection, where vascular occlusion was prominent (34).

The early steps of WST11 VTP and non–tumor-tissue response in organs

Figure 5

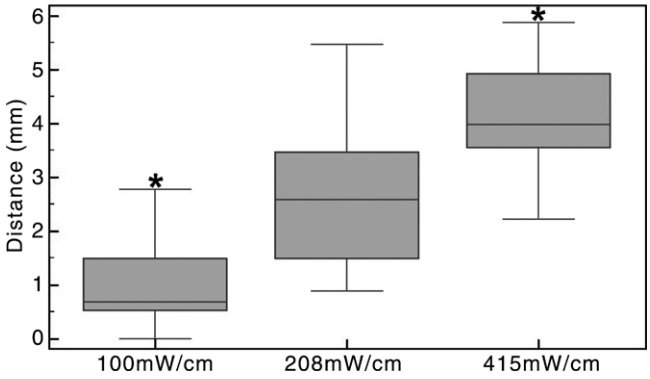

Figure 5: Plots of the distance to the first viable portal tract from the illuminating laser fiber in liver lesions 24 hours after WST11 VTP. At 100 mW (n = 29; mean, 0.96 mm; median, 0.69 mm; IQR, 0.53–1.49 mm), 200 mW (n = 30; mean, 2.64 mm; median, 2.59 mm; IQR, 1.49–3.47 mm), and 415 mW (n = 30; mean, 4.20 mm; median, 3.99 mm; IQR, 3.55–4.92 mm), increases in laser fluence increased the region in which small portal tract blood vessels (≤40 μm) remained unablated. * = statistical significance ($P < .0001$ with the Mann-Whitney rank sum test).

other than the prostate that are targets for focal therapy have not been resolved previously. These early events critically define treatment safety and selectivity and complement the large body of data concerning the early tumor response to WST11 VTP in small-animal tumor-bearing models. The histopathologic analysis presented in our study showed selective, nonthermal CN as the primary mechanism of cell death in normal tissues.

For both single and multiple laser fiber arrangements, WST11 VTP resulted in consistent and reproducible ablations that were clearly delineated from the nontreated tissue as early as 4 hours after treatment. The 1, 2, 3, 5-triphenyltetrazolium chloride viability staining of gross specimens, cell morphology with H-E staining, early DNA fragmentation that manifested with positive TUNEL staining, and lack of apoptotic bodies and dynamic cleaved caspase-3 expression patterns all indicate that the tissues within the ablation zone are committed to the pathway of cellular CN. By 24 hours after treatment, complete necrosis of parenchymal cells had occurred in the central region, as well as in the surrounding HZ and ATN regions in liver and kidney, respectively.

CN is a descriptive histopathologic finding induced by thermal tissue damage, ischemia, or irreversible hypoxia as a result of embolization procedures or, more acutely, by ischemia-reperfusion injury (35,37). WST11 VTP did not generate a clinically significant temperature change (defined here as $\Delta T \geq 8°C$, since some coagulation effects are expected with extended animal tissue heating to >45°C) at less than 208 mW/cm and did not obstruct vessels by means of thrombotic processes, as no intravascular fibrin deposition was observed. Therefore, our data support findings from previous preclinical models that showed that intravascular reactive oxygen species generation and propagation of tissue effects occur through a mechanism similar to ischemia-reperfusion injury. This corroborates other mechanisms presented for WST11 VTP of tumors in small-animal models (28).

In stark contrast to perivascular cellular sparing often seen with thermal ablation mechanisms (13), WST11 VTP performed under therapeutic conditions provides complete necrosis of all perivascular cells within the treatment zone while sparing midsize (40–200-μm) and large (>200-μm) vessels of nontumor tissues. Considering our previously published data (36), vessels of normal tissues appear to be more resistant to WST11 VTP than tumor-associated vessels. In the absence of oxygen, photo-excited WST11 undergoes nonradiative decay to the ground state. As the number of excited molecules increases, increased heat dissipation by nonradiative decay of the excited molecules results in the observed temperature increase.

Several putative mechanisms for the difference between normal and tumor vessel response may be considered. These include differences in tumor vessel permeability, dependency on hypoxia-related pathways in cancer microenvironments, aberrant expression of ischemia-reperfusion mediators in tumor endothelial cells, and mechanisms of hypoxia resistance in normal vessels, even at high light energy. Such areas require further investigation.

Lastly, our finding of infiltration by acute and then chronic inflammatory cells after WST11 VTP is consistent with data gathered from the clinical trials in prostate cancer mentioned earlier (28,31), where biopsy samples obtained 6 months after VTP treatment demonstrated macrophages and giant cells in the ablated regions (29). Persistence of a low-level and prolonged inflammatory response should contribute to the processes of immune education and the development of antitumor immunity (30). Moreover, viable blood vessels within the ablation provide portals for inflammatory cell infiltration, in response to the acute nonthermal cellular necrosis. Necrotic cell releases of nondenatured RNA and DNA and various antigens is expected to enhance innate and prolonged immunity, as we reported from the tumor-bearing small-animal models (21,30).

Irreversible electroporation is another nonthermal ablation modality that has been clinically adopted for the local treatment of tumors at locations where the use of traditional thermal ablation techniques are contraindicated for safety or effectiveness reasons (38). Similar to VTP, irreversible electroporation can be applied adjacent to

blood vessels without being affected by the heat-sink effect and has been reported to spare medium-large blood vessels in the vicinity of the ablation, with no visible effect on collagenous extracellular matrix (39). However, irreversible electroporation of tumors requires the application of high-voltage electric pulses into tissue, and the resulting electric field can cause severe neuromuscular activation and unintended cardiac stimulation. To avoid these unwanted side effects, patients undergoing irreversible electroporation have to be placed under deep sedation and require neuromuscular paralysis. Additionally, the energy can only be delivered safely with electrocardiographic gating, and this therapeutic technique is not suitable for use in patients with existing cardiac conditions. Therefore, when used in patients, VTP may provide the advantage of fewer safety considerations than irreversible electroporation, while preserving the benefits of a nonthermal ablation technique.

This study was limited to the use of animal tissues that were also non–tumor bearing, as no such large-animal models exist. Extrapolation to human tissues has been implied. Duration of follow-up was relatively brief and, though a longer time period may have provided data on tissue remodeling after treatment, additional information on tissue injury effects was not likely to be seen.

In conclusion, WST11 VTP treatment in the liver and kidneys produces a nonthermal form of complete tissue ablation, the depth of which is dependent on light intensity and characterized by uniform CN with preservation of tissue collagen scaffolding, blood vessels at least 40 μm in diameter, and surrounding stroma. These effects appear favorable for maintenance of normal organ function and recovery after treatment and provide important information for expectations regarding treatment effects in sensitive tissues and for contrasting this form of therapy to other ablation modalities. This study provides important clinical information on tissue effects from nonthermal ablation with WST11 VTP and is expected to lead to new guidelines for tumor ablation in sensitive anatomic domains. Such guidelines are particularly important in cases where the collagen scaffold and bystander vessels should maintain integrity and functionality. This includes, but is not limited to, prostate tissue ablation near the nerve bundle and ablation of pancreatic cancer and cancers in endoluminal cavities, such as the upper urinary tract or esophagus. The emerging role of tumor tissue ablation as a means to promote immune response in combination with immune-modulating techniques underscores the possible utility of this local ablation approach in the setting of disseminated diseases.

Acknowledgment: The authors gratefully acknowledge the Wade Thompson Family Foundation for their support.

Disclosures of Conflicts of Interest: S.Y.K. disclosed no relevant relationships. **T.V.T.** disclosed no relevant relationships. **S.M.** disclosed no relevant relationships. **G.S.** disclosed no relevant relationships. **D.G.** disclosed no relevant relationships. **J.C.D.** Activities related to the present article: disclosed no relevant relationships. Activities not related to the present article: author received a grant from the Thompson Family Foundation. Other relationships: disclosed no relevant relationships. **S.B.S.** Activities related to the present article: institution received a grant from the Thompson Foundation. Activities not related to the present article: author received payment from Devicor for board membership; author received payment from GE Healthcare and Johnson & Johnson for consulting; institution received grants from AngioDynamics. Other relationships: disclosed no relevant relationships. **P.T.S.** Activities related to the present article: disclosed no relevant relationships. Activities not related to the present article: author has stock options in OPKO; author received personal fees from Medivation for consulting. Other relationships: disclosed no relevant relationships. **A.S.** Activities related to the present article: author received a grant from the Wade Thompson Foundation; author received nonfinancial support from Steba-Biotech in the form of drugs and lasers. Activities not related to the present article: disclosed no relevant relationships. Other relationships: author has two patents. **J.C.** disclosed no relevant relationships.

References

1. Berland LL, Silverman SG, Gore RM, et al. Managing incidental findings on abdominal CT: white paper of the ACR incidental findings committee. J Am Coll Radiol 2010;7(10):754–773.
2. Esserman LJ, Thompson IM Jr, Reid B. Overdiagnosis and overtreatment in cancer: an opportunity for improvement. JAMA 2013;310(8):797–798.
3. Ahmed M, Brace CL, Lee FT Jr, Goldberg SN. Principles of and advances in percutaneous ablation. Radiology 2011;258(2):351–369.
4. Coleman JA, Scardino PT. Targeted prostate cancer ablation: energy options. Curr Opin Urol 2013;23(2):123–128.
5. Cordeiro ER, Cathelineau X, Thüroff S, Marberger M, Crouzet S, de la Rosette JJ. High-intensity focused ultrasound (HIFU) for definitive treatment of prostate cancer. BJU Int 2012;110(9):1228–1242.
6. Gervais DA, McGovern FJ, Arellano RS, McDougal WS, Mueller PR. Renal cell carcinoma: clinical experience and technical success with radio-frequency ablation of 42 tumors. Radiology 2003;226(2):417–424.
7. Gillams AR, Lees WR. Five-year survival following radiofrequency ablation of small, solitary, hepatic colorectal metastases. J Vasc Interv Radiol 2008;19(5):712–717.
8. Janzen NK, Han KR, Perry KT, Said JW, Schulam PG, Belldegrun AS. Feasibility of nerve-sparing prostate cryosurgery: applications and limitations in a canine model. J Endourol 2005;19(4):520–525.
9. Weld KJ, Hruby G, Humphrey PA, Ames CD, Landman J. Precise characterization of renal parenchymal response to single and multiple cryoablation probes. J Urol 2006;176(2):784–786.
10. Brinck H, Werner J. Efficiency function: improvement of classical bioheat approach. J Appl Physiol (1985) 1994;77(4):1617–1622.
11. Jiang F, He M, Liu YJ, Wang ZB, Zhang L, Bai J. High intensity focused ultrasound ablation of goat liver in vivo: pathologic changes of portal vein and the "heat-sink" effect. Ultrasonics 2013;53(1):77–83.
12. Gazelle GS, Goldberg SN, Solbiati L, Livraghi T. Tumor ablation with radio-frequency energy. Radiology 2000;217(3):633–646.
13. Gravante G. Thermal ablation for unresectable liver tumours, time to move forward? World J Gastrointest Surg 2010;2(1):1–5.
14. Wright AS, Sampson LA, Warner TF, Mahvi DM, Lee FT Jr. Radiofrequency versus microwave ablation in a hepatic porcine model. Radiology 2005;236(1):132–139.
15. Yu T, Luo J. Adverse events of extracorporeal ultrasound-guided high intensity focused ultrasound therapy. PLoS One 2011;6(12):e26110.

16. Brandis A, Mazor O, Neumark E, Rosenbach-Belkin V, Salomon Y, Scherz A. Novel water-soluble bacteriochlorophyll derivatives for vascular-targeted photodynamic therapy: synthesis, solubility, phototoxicity and the effect of serum proteins. Photochem Photobiol 2005;81(4):983–993.

17. Fabre MA, Fuseau E, Ficheux H. Selection of dosing regimen with WST11 by Monte Carlo simulations, using PK data collected after single IV administration in healthy subjects and population PK modeling. J Pharm Sci 2007;96(12):3444–3456.

18. Mazor O, Brandis A, Plaks V, et al. WST11, a novel water-soluble bacteriochlorophyll derivative; cellular uptake, pharmacokinetics, biodistribution and vascular-targeted photodynamic activity using melanoma tumors as a model. Photochem Photobiol 2005;81(2):342–351.

19. Goldschmidt R. The photochemical and biochemical processes that drive vascular targeted photodynamic therapy using water soluble bacteriochlorophyll derivatives [master's thesis]. Rehovot, Israel: Weizmann Institute, 2011.

20. Preise D, Scherz A, Salomon Y. Antitumor immunity promoted by vascular occluding therapy: lessons from vascular-targeted photodynamic therapy (VTP). Photochem Photobiol Sci 2011;10(5):681–688.

21. Dougherty TJ, Gomer CJ, Henderson BW, et al. Photodynamic therapy. J Natl Cancer Inst 1998;90(12):889–905.

22. Godoy H, Vaddadi P, Cooper M, Frederick PJ, Odunsi K, Lele S. Photodynamic therapy effectively palliates gynecologic malignancies. Eur J Gynaecol Oncol 2013;34(4):300–302.

23. Juarranz A, Jaén P, Sanz-Rodríguez F, Cuevas J, González S. Photodynamic therapy of cancer. Basic principles and applications. Clin Transl Oncol 2008;10(3):148–154.

24. Moan J, Peng Q. An outline of the hundred-year history of PDT. Anticancer Res 2003;23(5A):3591–3600.

25. Qumseya BJ, David W, Wolfsen HC. Photodynamic therapy for Barrett's esophagus and esophageal carcinoma. Clin Endosc 2013;46(1):30–37.

26. Ross K, Cherpelis B, Lien M, Fenske N. Spotlighting the role of photodynamic therapy in cutaneous malignancy: an update and expansion. Dermatol Surg 2013;39(12):1733–1744.

27. Yoo JO, Ha KS. New insights into the mechanisms for photodynamic therapy-induced cancer cell death. Int Rev Cell Mol Biol 2012;295:139–174.

28. Coleman JA, Scherz A. Focal therapy of localised prostate cancer by vascular targeted photodynamic therapy with WST-11 (TOOKAD®Soluble). Eur Urol Rev 2012;7(2):106–108.

29. Eymerit-Morin C, Zidane M, Lebdai S, Triau S, Azzouzi AR, Rousselet MC. Histopathology of prostate tissue after vascular-targeted photodynamic therapy for localized prostate cancer. Virchows Arch 2013;463(4):547–552.

30. Preise D, Oren R, Glinert I, et al. Systemic antitumor protection by vascular-targeted photodynamic therapy involves cellular and humoral immunity. Cancer Immunol Immunother 2009;58(1):71–84.

31. Azzouzi AR, Barret E, Moore CM, et al. TOOKAD® Soluble vascular-targeted photodynamic (VTP) therapy: determination of optimal treatment conditions and assessment of effects in patients with localised prostate cancer. BJU Int 2013;112(6):766–774.

32. Fleshker S, Preise D, Kalchenko V, Scherz A, Salomon Y. Prompt assessment of WST11-VTP outcome using luciferase transfected tumors enables second treatment and increase in overall therapeutic rate. Photochem Photobiol 2008;84(5):1231–1237.

33. Gavrieli Y, Sherman Y, Ben-Sasson SA. Identification of programmed cell death in situ via specific labeling of nuclear DNA fragmentation. J Cell Biol 1992;119(3):493–501.

34. Chevalier S, Cury FL, Scarlata E, et al. Endoscopic vascular targeted photodynamic therapy with the photosensitizer WST11 for benign prostatic hyperplasia in the preclinical dog model. J Urol 2013;190(5):1946–1953.

35. Zong WX, Thompson CB. Necrotic death as a cell fate. Genes Dev 2006;20(1):1–15.

36. Madar-Balakirski N, Tempel-Brami C, Kalchenko V, et al. Permanent occlusion of feeding arteries and draining veins in solid mouse tumors by vascular targeted photodynamic therapy (VTP) with Tookad. PLoS One 2010;5(4):e10282.

37. Kroemer G, Galluzzi L, Vandenabeele P, et al. Classification of cell death: recommendations of the Nomenclature Committee on Cell Death 2009. Cell Death Differ 2009;16(1):3–11.

38. Neal RE 2nd, Singh R, Hatcher HC, Kock ND, Torti SV, Davalos RV. Treatment of breast cancer through the application of irreversible electroporation using a novel minimally invasive single needle electrode. Breast Cancer Res Treat 2010;123(1):295–301.

39. Charpentier KP. Irreversible electroporation for the ablation of liver tumors: are we there yet? Arch Surg 2012;147(11):1053–1061.